



Influence of carbon addition on mechanical properties of Fe–Mn–C twinning-induced plasticity steels

Peng Fu¹ · Zhi-bing Zheng³ · Wei-ping Yang¹ · Hao-kun Yang²

Received: 15 April 2021 / Revised: 22 June 2021 / Accepted: 24 June 2021 / Published online: 14 November 2021
© China Iron and Steel Research Institute Group 2021

Abstract

Mechanical properties and microstructural evolution of Fe–22Mn–0.6C and Fe–22Mn–1.0C (wt.%) twinning-induced plasticity (TWIP) steels were investigated by monotonic, stress-relaxation and unloading–reloading tensile tests. The dynamic strain aging (DSA) effect, resulting from pinning of dislocations, effectively improved the dislocation activation volume of the two TWIP steels. In the meanwhile, DSA-facilitated twinning nucleation mechanism kept similar twinning capabilities of the two TWIP steels. With strain increasing, the formation of high-density deformation twins restricted the dislocation motion and reduced the activation volume with increasing strain. Furthermore, C addition simultaneously improved the ultimate tensile strength and uniform elongation, and significantly enhanced the friction stress, rather than back stress. The stronger short-range order effect, brought by friction stress, promotes the planar dislocation slipping, thus improving the work-hardening capability. As a result, the additional work-hardening capacity can be achieved in Fe–Mn–C with higher C addition.

Keywords Twinning-induced plasticity steel · Work-hardening rate · Dynamic strain aging · Short-range order · Deformation twin

1 Introduction

In the past years, the simultaneous improvement of ultimate tensile stress and uniform elongation has been achieved by introducing nano-scale deformation twins (DTs) during the plastic deformation [1, 2]. These continuous formed nano-scale DTs divide the grains into smaller domains with further strain, thus reducing the dislocation mean free path and leading to dynamic Hall–Petch effect

[3]. Among various materials systems, twinning-induced plasticity (TWIP) steel has drawn much attention due to their superior combination of strength and ductility, outstanding twinning capability, as well as energy saving advantages [4–7]. Recently, the third-generation advanced high-strength steel was proposed, especially the transformation-induced plasticity steel was developed with optimization of strength-ductility combination [8].

The twinning capability is supposed to be related to the stacking fault energy (SFE), which can be changed by alloying addition [9, 10]. For example, the additions of Al and Zn into Cu alloys are proved to reduce SFE of alloys, thus the twinning capability is improved, and the work-hardening rate becomes synchronously increasing [11]. In contrast, the addition of Al element into Fe–Mn–C TWIP steel significantly increases SFE of material, subsequently suppressing the formation of DTs [10, 12]. It thus appears that the occurrence of DTs is dependent on SFE [13], where the twinning nucleation and growth can be promoted in metallic materials with lower SFE [14]. Following the pronounced twinning capability by decreasing SFE, the work-hardening rate should be enhanced synchronously,

✉ Wei-ping Yang
wp_yang1@126.com

✉ Hao-kun Yang
hkyang@hkpc.org

¹ School of Engineering, Jiangxi Agricultural University, Nanchang 330045, Jiangxi, China

² Smart Manufacturing Division, Hong Kong Productivity Council, Hong Kong 999077, China

³ Institute of New Materials, Guangdong Academy of Sciences, Guangdong Provincial Iron Matrix Composite Engineering Research Center, Guangzhou 510650, Guangdong, China

leading to the excellent balance of strength and ductility [13].

However, the recent studies reported that SFE of Fe–Mn–C TWIP steels increases by the addition of C element, with a positive slope of 38.3 mJ m^{-2} per 1 wt.% C [15, 16]. Meanwhile, the mechanical properties and work-hardening capability are enhanced unexpectedly [17, 18]. These findings demonstrate that SFE-dependent twinning mechanism seems to expire in Fe–Mn–C TWIP steel, and the underlying mechanism needs further investigation. Furthermore, the previous studies pointed out that the dynamic strain aging (DSA) effect also plays an important role in twinning capability and fracture mechanism [19, 20]. Hence, DSA effect on the mechanical properties will also be investigated. In the present study, we carry out stress-relaxation and unloading–reloading tensile tests, and electron channeling contrast imaging (ECCI) and transmission electron microscopy (TEM) observations to investigate the mechanical properties, work-hardening and microstructural evolutions of Fe–22Mn–0.6C and Fe–22Mn–1.0C (wt.%) austenitic TWIP steels. The present study aims to reveal the mechanism of C addition on the strengthening effect and work-hardening behavior of Fe–Mn–C TWIP steel.

2 Material and methods

The ingots of Fe–22Mn–0.6C (denoted as 0.6C, wt.%) and Fe–22Mn–1.0C (denoted as 1.0C, wt.%) TWIP steels were prepared in vacuum induction furnace and austenitized at 1423 K for 2 h. Later, the ingots were hot-forged into square bar with final section of $25 \text{ mm} \times 25 \text{ mm}$ over 1123 K. The square bars were annealed at 1273 K for 30 min and immediately quenched in water to obtain fully recovery structure. SFEs of 0.6C and 1.0C steels are measured to be 19 and 32 mJ m^{-2} [16], indicating that SFE increases with increasing C content. The tensile tests were carried out using INSTRON 5982 testing machine with strain rate of 10^{-3} s^{-1} and room temperature. The stress-relaxation tests were strained up to certain strains, then the crosshead was fixed, and stress was recorded with time between 20 and 40 s. The unloading–reloading tests were performed in a displacement-control mode with an unloading rate of -0.9 mm min^{-1} . All the tensile tests are recorded by an extensometer and repeated at least twice to avoid artificial error.

The microstructures of as-received 0.6C and 1.0C TWIP steels were detected under optical microscope, and the average grain sizes of 0.6C and 1.0C TWIP steels were measured to be 40 and $31 \mu\text{m}$ without consideration of annealing twin boundaries, and 32 and $26 \mu\text{m}$ with consideration of twin boundaries, as illustrated in Fig. 1a and

b. As the average grain sizes of the two TWIP steels are close, the Hall-Perch relation on yield stress variation will not be discussed here. The deformed samples of 0.6C and 1.0C TWIP steels were observed under LEO supra 55 field emission scanning electron microscope (SEM) equipped with an ECCI system operating at 20 kV, and FEI Tecnai F20 TEM, operating at 200 kV. The as-received and fractured 0.6C and 1.0C TWIP steel samples were examined by X-ray diffraction (XRD), where no phase transformation was detected in both materials after fracture, as shown in Fig. 1c and d. In the previous study by XRD, no phase change was detected after straining [21].

3 Results and discussion

3.1 Mechanical properties

The true stress–strain tensile and work-hardening rate ($\partial\sigma/\partial\varepsilon$) curves of these two TWIP steels are illustrated in Fig. 2. The yield stress of 1.0C steel (378 MPa) is slightly higher than that of 0.6C steel (348 MPa), resulting from C solid solution contributions. In the previous study, Shao et al. [22] point out that the addition of C element in Fe–Mn–C TWIP will introduce 180 MPa improvement per 1 wt.% of C element. Besides, the grain sizes of 0.6C and 1.0C TWIP steels are close, so that the influence from grain size on the flow stress will be ignored in the present study. Therefore, the difference of yield stress ($\sim 30 \text{ MPa}$) shall be from C addition difference, and the effects of grain size and C element addition on the flow stress won't be deeply discussed in the present study. With increasing strain, the flow stress of 1.0C steel gradually surpasses 0.6C steel. Moreover, the flow stress of 1.0C steel reaches 2145 MPa, which is much higher than that of 0.6C with 1848 MPa at fracture point. The work-hardening curves are shown in Fig. 2b. Overall, the work-hardening rate decreases firstly until a strain of 0.1 and then goes upwards with further increasing the strain. In addition, 1.0C steel always exhibits stronger work-hardening rate than 0.6C steel.

3.1.1 Stress–relaxation behaviors

As illustrated in Fig. 2a, the serrations are detected in both of two TWIP steels. These serrations should come from DSA effect, resulting from the repeating of pinning and unpinning of C atoms on partial dislocations [19]. To further explore the interaction between C atoms and dislocations in Fe–Mn–C system TWIP steel, the stress-relaxation tests are commonly accepted [6, 23]. Figure 3a and b provides the stress-relaxation tests of 0.6C [6] and 1.0C steels with strain and time, respectively. The magnification of stress-relaxation cycle at strains of 0.1, 0.3 and 0.45 are

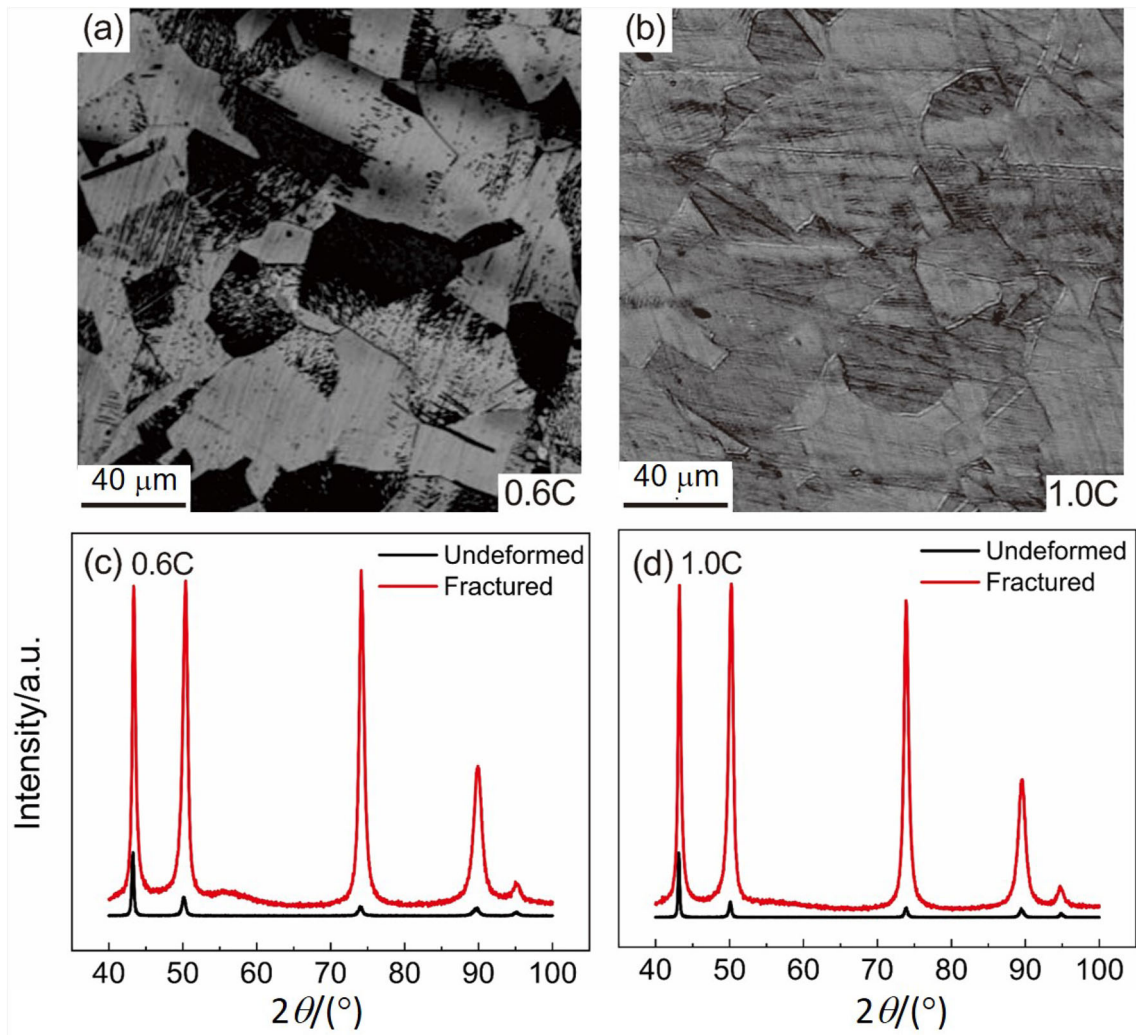


Fig. 1 Optical microscopy images of annealed 0.6C (a) and 1.0C (b) TWIP steels, and XRD results of 0.6C (c) and 1.0C (d) steels before and after tensile tests. 2θ Diffraction angle

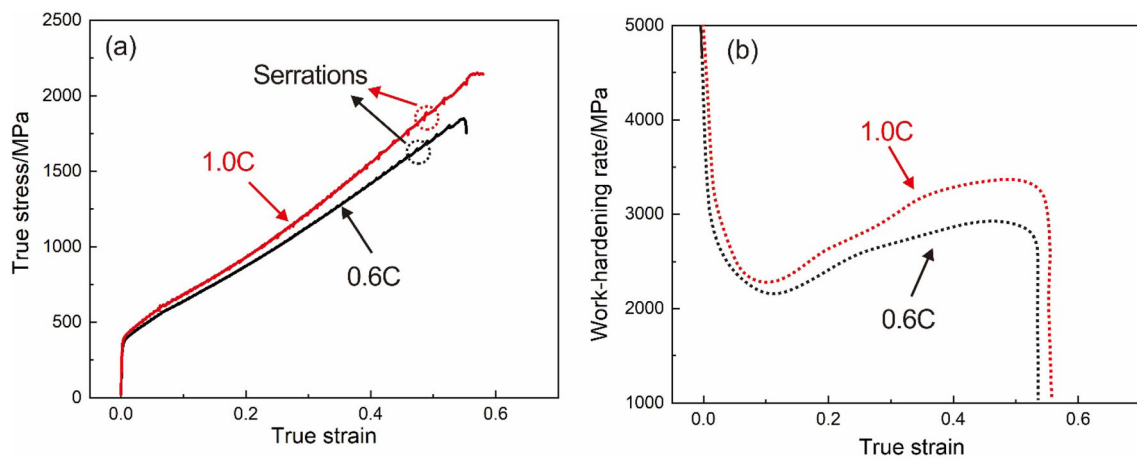


Fig. 2 Tensile true stress–strain curves (a) and work-hardening rates of 0.6C and 1.0C TWIP steels (b)

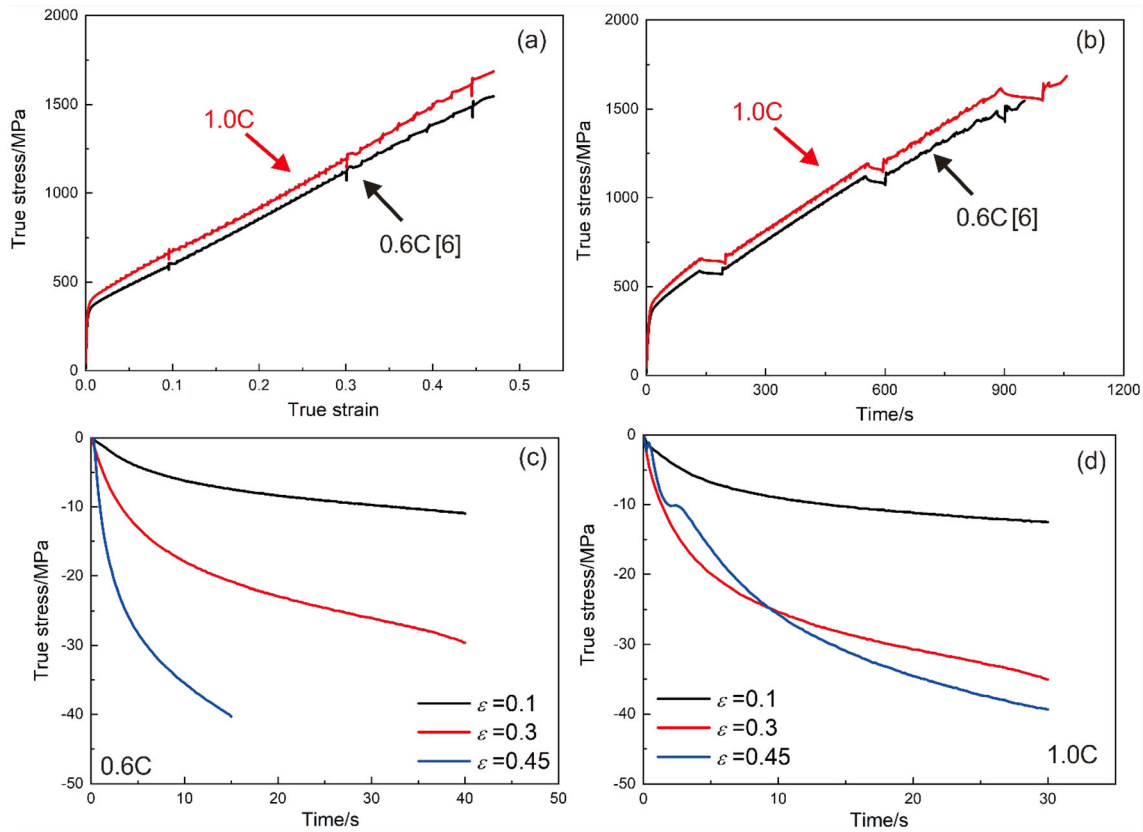


Fig. 3 Stress-relaxation curves of 0.6C [6] and 1.0C steels with strain (a) and time (b) as well as magnification of stress relaxation cycles at true strains of 0.1 and 0.3 with time (c, d)

presented in Fig. 3c and d, where the stress drops of the two steels get higher with strain, and the two steels exhibit similar degree of stress drop at the same strain. However, the detailed comparison needs to be done, for exploring the influence of C content on the dislocation pinning behavior.

Through the stress-relaxation tests, the value of activation volume (V_a), reflecting generalized area swept by a dislocation, can be directly obtained [24, 25]. The higher value of V_a indicated that the possibility of C atoms pinning on dislocations is higher [6, 23]. V_a is determined by fitting the stress-relaxation curve according to Eq. (1) [23, 25]:

$$\Delta\sigma = \frac{\sqrt{3}kT}{V_a} \ln\left(1 + \frac{t}{c}\right), \tag{1}$$

where k is the Boltzmann constant of $1.38 \times 10^{-23} \text{ J K}^{-1}$; T and t is temperature and time, respectively; c is fitting constant; and $\Delta\sigma$ is the flow stress drop with time.

The value V_a of 0.6C [6] and 1.0C TWIP steels are calculated and are shown in Fig. 4, where the values of V_a of the two steels are larger than $100 b^3$ at the early strain of 0.1. According to the previous studies [6, 23], the high value of V_a ($> 100 b^3$) represents the occurrence of DSA effect in the dislocation-mediated plastic deformation. It should be noted that V_a of 1.0C steel is larger, referring that

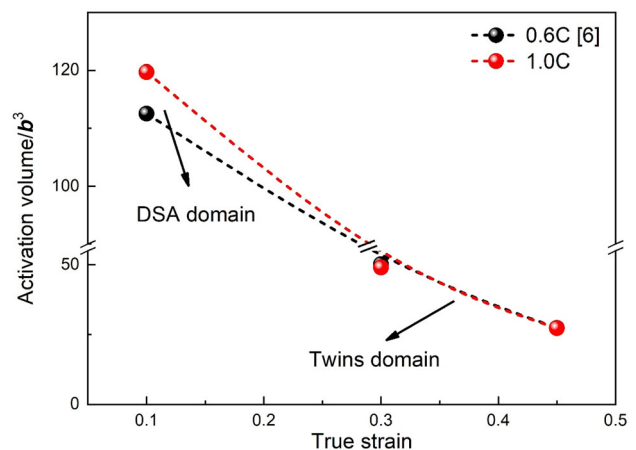


Fig. 4 Activation volumes of 0.6C [6] and 1.0C steels with strain

the larger area of pinned dislocations is activated. With strain increasing to 0.3, V_a of the two steels decreases to less than $50 b^3$. However, the decrease of V_a with strain cannot be attributed to DSA effect, where DSA effect works till fracture. To explain the decreasing V_a with strain, the detailed microstructure observation needs further investigation.

3.1.2 Unloading–reloading behaviors

According to the previous studies [26], the upward increase in work-hardening rate results from the nano-scale twin lamellas, which contributes high level of back stress to supporting the steadily increasing work-hardening rate. To reveal the mechanisms for the different mechanical responses in both steels, the unloading–reloading tensile tests were carried out to examine the back stress evolution with strain.

Figure 5a shows the unloading–reloading curves of 0.6C [6] and 1.0C steels, and Fig. 5b illustrates typical hysteresis loop curves. σ_{\max} and σ_{rev} (Fig. 5b) represent the stress just before unloading and the stress departs from linear stress–strain curve, respectively [27]. The departure value from linearity is denoted as $\Delta\varepsilon$, and the value of 2.5×10^{-4} is adopted [28]. The back stress (σ_b) and friction stress (σ_f) can be calculated as below [29, 30]:

$$\sigma_b = \frac{\sigma_{\max} + \sigma_{\text{rev}}}{2} \quad (2)$$

$$\sigma_f = \frac{\sigma_{\max} - \sigma_{\text{rev}}}{2} \quad (3)$$

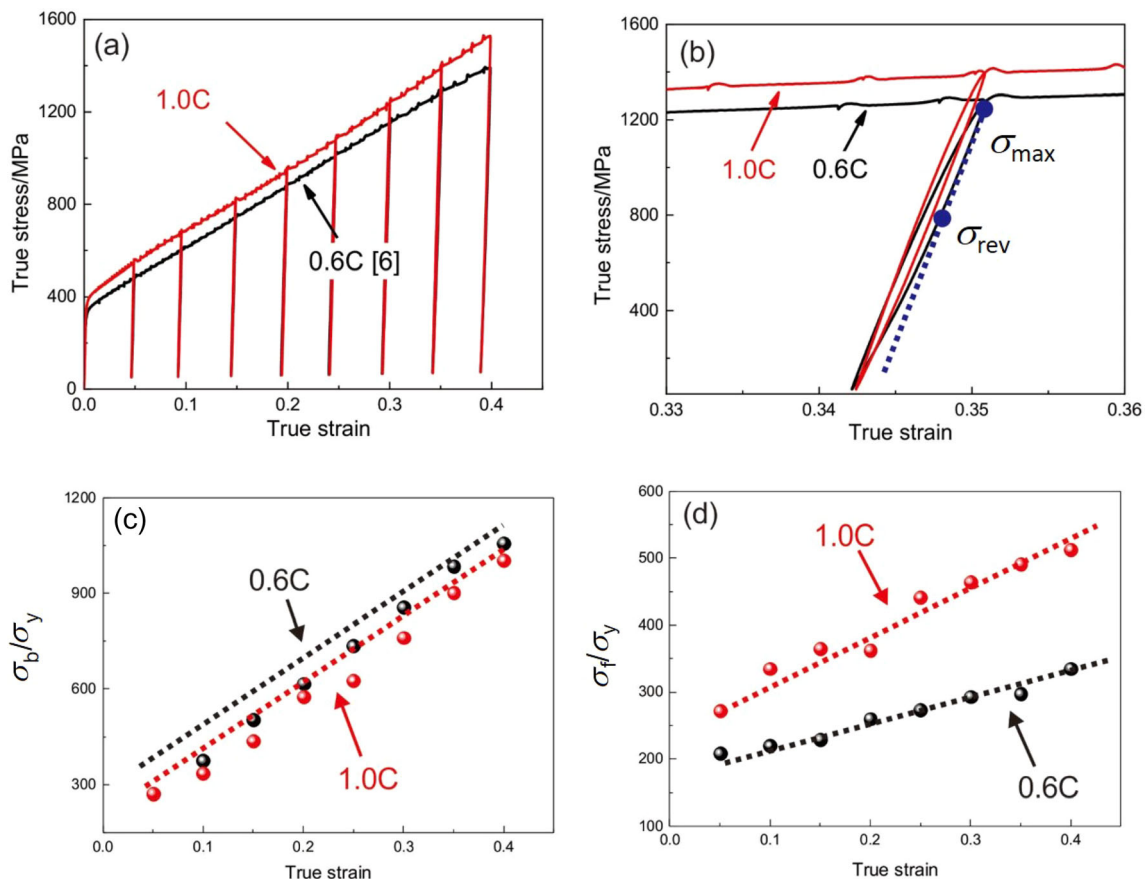


Fig. 5 Unloading–reloading curves of 0.6C [6] and 1.0C TWIP steels (**a**, **b**), and ratio of σ_b (**c**) and σ_f (**d**) to σ_y curves

To minimize the influence of grain size and solid solution hardening on the back stress and friction stress comparison, the ratio of back stress (and friction stress) to yield stress is adopted. Figure 5c illustrates σ_b/σ_y with strain, where no much difference is detected between 0.6C and 1.0C steels. It thus suggests that the twinning evolutions of the two steels should be more or less the same, because the back stress of TWIP steel mainly results from the interaction between dislocation gliding and DTs [31, 32]. Meanwhile, σ_f/σ_y in the two steels with strain are exhibited in Fig. 5d, where 1.0C steel possesses much higher level of friction stress than 0.6C steel, and the difference becomes more obvious with increasing the strain. The strain rate tests [19, 20] of Fe–Mn–C system steels reveal that the steel has negative strain rate sensitivity (the flow stress decreases with increasing strain rate), because the pinning of C atoms to dislocations is suppressed at high strain rate. These studies also support that C addition into Fe–Mn–C TWIP steels can improve the friction stress. The present results indicate that the stronger work-hardening capability of 1.0C TWIP steel should not be result from additional DTs, and the mechanism for higher dependence of friction stress on C content needs further investigation.

3.2 Microstructure evolution

Figure 6 provides TEM observations of dislocation patterns in 0.6C and 1.0C steels at true strains of 0.1 and 0.25, respectively. At the early strain of 0.1, 0.6C steel exhibits dislocation wavy slip characterization along with dislocation cell structures (Fig. 6a), but 1.0C steel exhibits typical dislocation planar slip (Fig. 6b). This transition of dislocation slip mode should be related with C content. It is reported that C addition into Fe–Mn–C TWIP steel introduces C–Mn clusters and brings short-range order (SRO) structure [33, 34]. Therefore, the dislocation motion is restricted along specific slip plane, promoting planar slip [19, 35], and this phenomenon is further confirmed by the higher planarity of dislocation slip in 1.0C steel. As deformation proceeds to a true strain of 0.25, the widely

developed dislocation cells (DCs) are observed in 0.6C steel (Fig. 6c). Instead, both dislocation planar slip and wavy slip are observed in 1.0C steel (Fig. 6d). The mixture of dislocation patterns in 1.0C steel should be related with the breakdown of SRO effect in 1.0C steel [22].

The nano-scale DTs are proved to play an important role in improving the back stress and work-hardening rate of TWIP steel [31, 32]. However, the present unloading–reloading tests reveal that the back stresses of 0.6C and 1.0C TWIP steels are comparable, indicating that the twinning evolution with strain should be relatively close in the two steels. To approve this viewpoint, the detailed morphologies of DTs under TEM are provided in Fig. 7. At the true strain of 0.25, nano-scale DTs are both observed in 0.6C (Fig. 7a) and 1.0C (Fig. 7b) steels. The corresponding selected-area diffraction pattern, inserted in Fig. 7a, proves

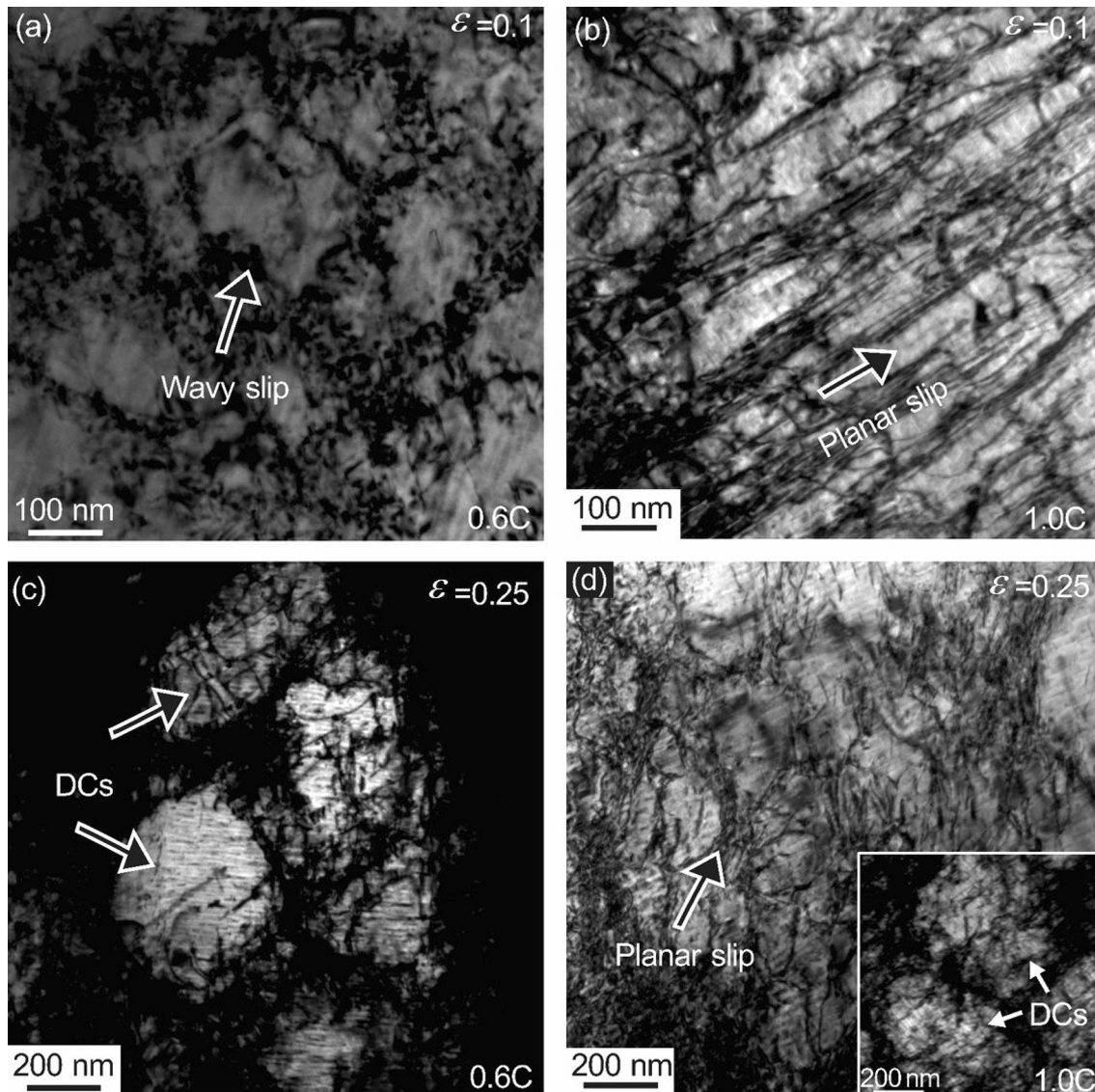


Fig. 6 TEM images of dislocations of 0.6C (a, c) and 1.0C (b, d) steels straining to true strains of 0.1 (a, b) and 0.25 (c, d)

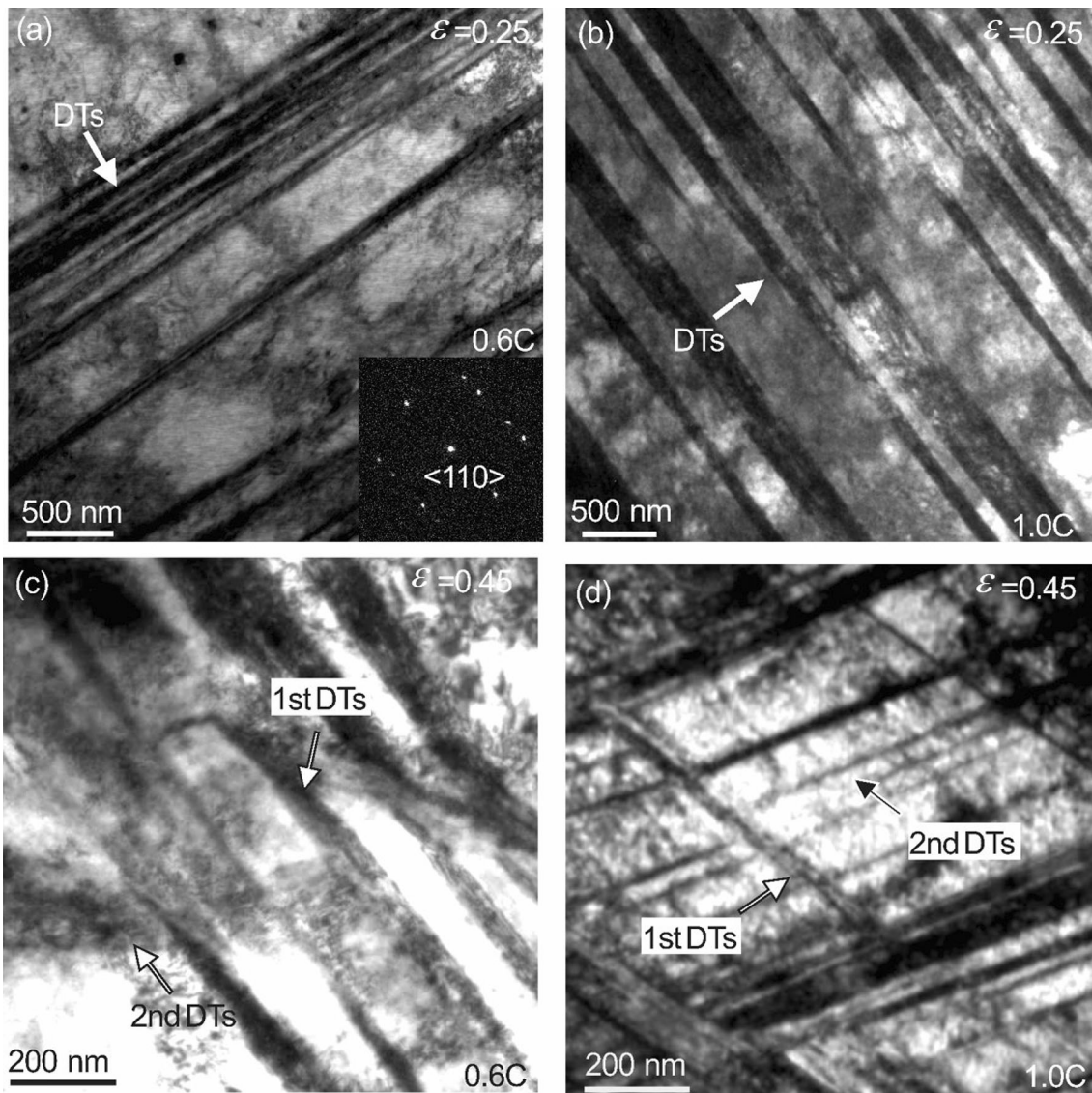


Fig. 7 TEM images of deformation twins of 0.6C (a, c) and 1.0C (b, d) steels straining to true strains of 0.25 (a, b) and 0.45 (c, d). Selected-area diffraction patterns of deformation twins is inserted in a along $\langle 110 \rangle$ zone axis orientation

that existence of DTs. With increasing the strain to 0.45, the spacing of DTs gets narrow in both steels (Fig. 7c and d). Besides, secondary DTs (2nd DTs) are also observed, and these profuse 2nd DTs further improve the work-hardening rate of TWIP steels with strain [36, 37], as shown in Fig. 2b. However, the present TEM observation reveals that the density of DTs is comparable in 0.6C and 1.0C TWIP steels.

The large-scale observations of DTs under ECCI are conducted and are shown in Fig. 8, where the twinned grain fractions (the definition can be found in Ref. [38]), in 0.6C and 1.0C steels, are measured to be 0.33, 0.56, 0.81 and 0.27, 0.43, 0.86 at true strains of 0.1, 0.25 and 0.45, respectively. The statistical results prove that the twinning capabilities in the two steels are close. Although SFE of

1.0C steel is higher, the stronger DSA-induced locking on trailing partial dislocation assists twinning nucleation. Hence, the twinning capability of 1.0C keeps as strong as 0.6C steel does [39]. Besides, the back stress measurement also supports the fact that the similar twinning capabilities of 0.6C and 1.0C steels contribute to comparable back stress, as shown in Fig. 5c. In addition, the decreasing activation volume of 0.6C and 1.0C TWIP steels with strain could be attributed to the formation of DTs [6, 40]. As illustrated in Fig. 7, DTs divide the grains into nano-size domains, where the dislocations are restricted. Thus, the area swept by dislocations drops at higher strain, for the increasing density of DT.

As discussed above, the higher work-hardening rate of 1.0C steel than 0.6C steel should not originate from the

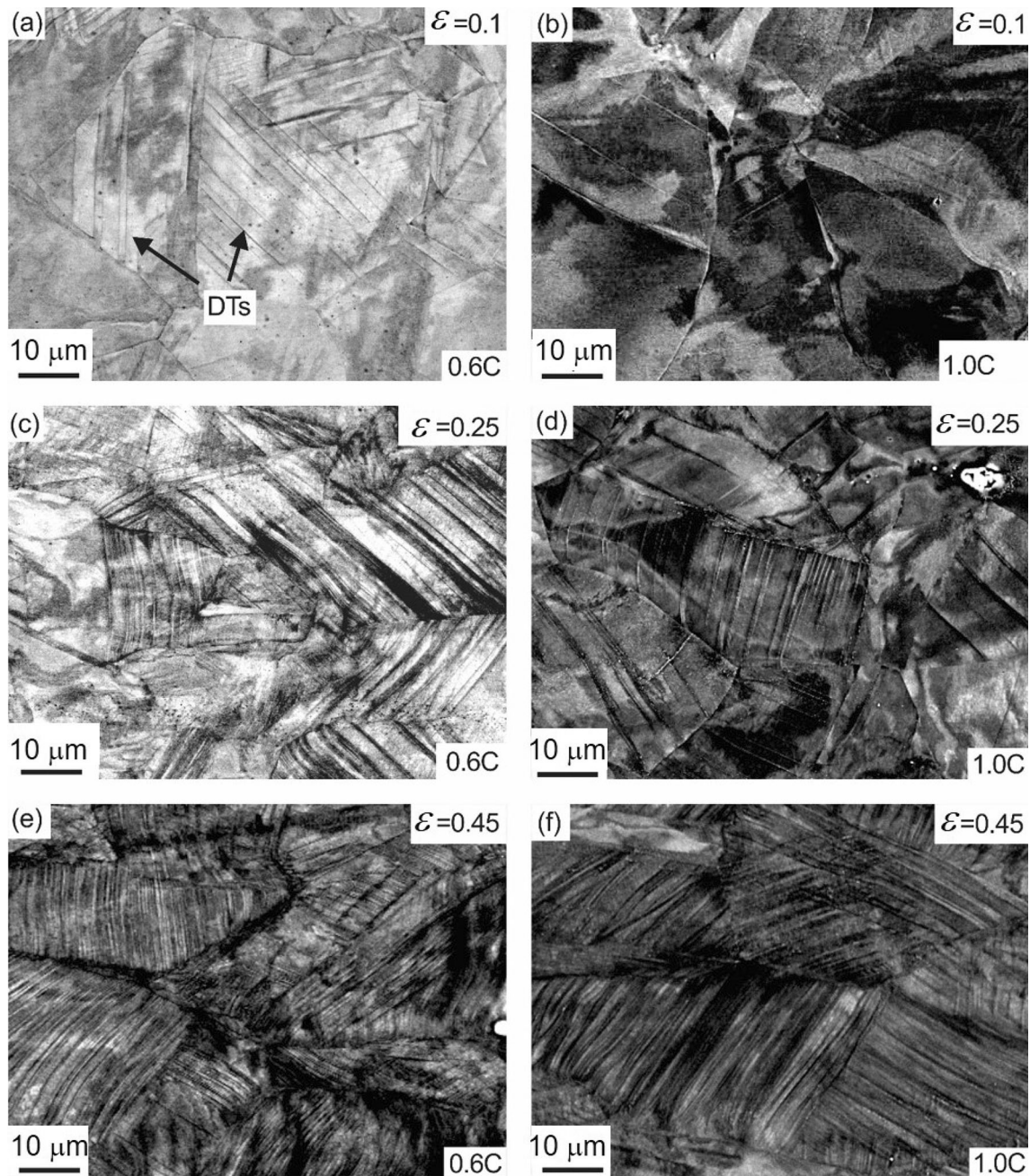


Fig. 8 ECCI observation of 0.6C (a, c, e) and 1.0C (b, d, f) TWIP steels tensioned to true strains of 0.1 (a, b), 0.25 (c, d), and 0.45 (e, f)

DTs, because the twinning capabilities of 0.6C and 1.0C steels are similar. The enhanced flow stress and work-hardening capability with increasing C addition should be closely connected with the friction stress. The interstitial solid solution atoms hinder the dislocation cross slipping and suppress the dislocation dynamic recovery [35, 41]. Then, the dislocation density increases, leading to strong dislocation hardening effect [42, 43]. Furthermore, the strength contribution from dislocation planar slipping is higher than that from wavy slipping [44]. Consequently,

the flow stress is higher and work-hardening rate continues to grow in 1.0C steel. This strengthening mechanism also works in nano-twinned Cu [45].

4 Conclusions

In this work, the mechanical responses under monotonic, stress–relaxation and unloading–reloading tests were investigated in 0.6C and 1.0C TWIP steels. DSA effect in

0.6C and 1.0C TWIP steels is confirmed to be resulted from the pinning of C atoms on dislocations. DSA-facilitated twinning behavior is considered to work in Fe–Mn–C system TWIP steel. As the activation volume of 1.0C steel is higher at early strain, DSA-facilitated twinning behavior further promotes the twinning nucleation. Therefore, 1.0C and 0.6C TWIP steels exhibit similar twinning capability, while 1.0C TWIP steel has a higher SFE than 0.6C steel. The increasing density of DTs constrains the dislocation motion, resulting in the decreasing of activation volume.

The unloading–reloading tests reveal that the back stress values are comparable for the two steels, which is resulted from the similar twinning capability. However, the friction stress of 1.0C steel is much higher than that of 0.6C steel, and this is further pronounced with increasing the strain. The higher friction stress of 1.0C steel, resulted from the solid solution effect and planarity dislocation slip mode via SRO effect, leads to the higher work-hardening rate and flow stress.

Acknowledgements The authors would like to thank Prof. Zhe-feng Zhang and Prof. Yan-zhong Tian from Institute of Metal Research, Chinese Academy Sciences of Sciences for fruitful discussion. The authors do not have any possible conflicts of interest. This work was supported by International Science and Technology Cooperation Project of Guangdong Province (No. 2021A0505030051), Guangdong Academy of Science (No. 2021GDASYL-20210102002).

References

- [1] L. Lu, X. Chen, X. Huang, K. Lu, *Science* 323 (2009) 607–610.
- [2] Y.T. Zhu, X. Liao, *Nat. Mater.* 3 (2004) 351–352.
- [3] Y. Wu, D. Tang, H. Jiang, Z. Mi, H. Jing, *Acta Metall. Sin. (Engl. Lett.)* 26 (2013) 713–720.
- [4] P. Zhou, M.X. Huang, *Metall. Mater. Trans. A* 46 (2015) 5080–5090.
- [5] Z.L. Mi, D. Tang, L. Yan, J. Guo, *J. Mater. Sci. Technol.* 21 (2005) 451–454.
- [6] H.K. Yang, Y.Z. Tian, Z.F. Zhang, *Mater. Sci. Eng. A* 731 (2018) 61–70.
- [7] L. Li, *Mater. Res. Appl.* 2 (2008) 328–331.
- [8] M. Soleimani, A. Kalhor, H. Mirzadeh, *Mater. Sci. Eng. A* (2020) 140023.
- [9] S. Allain, J.P. Chateau, O. Bouaziz, S. Migot, N. Guelton, *Mater. Sci. Eng. A* 387–389 (2004) 158–162.
- [10] A. Dumay, J.P. Chateau, S. Allain, S. Migot, O. Bouaziz, *Mater. Sci. Eng. A* 483–484 (2008) 184–187.
- [11] R. Liu, Z.J. Zhang, L.L. Li, X.H. An, Z.F. Zhang, *Sci. Rep.* 5 (2015) 9550.
- [12] K.T. Park, K.G. Jin, S.H. Han, S.W. Hwang, K. Choi, C.S. Lee, *Mater. Sci. Eng. A* 527 (2010) 3651–3661.
- [13] J.E. Jin, Y.K. Lee, *Acta Mater.* 60 (2012) 1680–1688.
- [14] T.S. Byun, *Acta Mater.* 51 (2003) 3063–3071.
- [15] J. Nakano, P.J. Jacques, *Calphad* 34 (2010) 167–175.
- [16] A. Saeed-Akbari, J. Imlau, U. Prahl, W. Bleck, *Metall. Mater. Trans. A* 40 (2009) 3076–3090.
- [17] S. Liu, L. Qian, J. Meng, P. Ma, F. Zhang, *Mater. Sci. Eng. A* 639 (2015) 425–430.
- [18] M. Huang, O. Bouaziz, D. Barbier, S. Allain, *J. Mater. Sci.* 46 (2011) 7410–7414.
- [19] S.J. Lee, J. Kim, S.N. Kane, B.C.D. Cooman, *Acta Mater.* 59 (2011) 6809–6819.
- [20] A. Bintu, G. Vincze, C.R. Picu, A.B. Lopes, J.J. Grácio, F. Barlat, *Mater. Sci. Eng. A* 629 (2015) 54–59.
- [21] H.K. Yang, Z.J. Zhang, Y.Z. Tian, Z.F. Zhang, *Mater. Sci. Eng. A* 690 (2017) 146–157.
- [22] C.W. Shao, P. Zhang, R. Liu, Z.J. Zhang, J.C. Pang, Z.F. Zhang, *Acta Mater.* 103 (2016) 781–795.
- [23] O. Majidi, B.C. De Cooman, F. Barlat, M.G. Lee, Y.P. Korkolis, *Mater. Sci. Eng. A* 674 (2016) 276–285.
- [24] X.S. Yang, Y.J. Wang, G.Y. Wang, H.R. Zhai, L.H. Dai, T.Y. Zhang, *Acta Mater.* 108 (2016) 252–263.
- [25] F. Guiu, P.L. Pratt, *Phys. Status Solidi* 6 (1964) 111–120.
- [26] J. Gil Sevillano, F. de las Cuevas, *Scripta Mater.* 66 (2012) 978–981.
- [27] J.I. Dickson, J. Boutin, L. Handfield, *Mater. Sci. Eng.* 64 (1984) L7–L11.
- [28] H.K. Yang, V. Doquet, Z.F. Zhang, *Mater. Sci. Eng. A* 672 (2016) 7–14.
- [29] M. Yang, Y. Pan, F. Yuan, Y. Zhu, X. Wu, *Mater. Res. Lett.* 4 (2016) 145–151.
- [30] I. Gutierrez-Urrutia, J.A. del Valle, S. Zaefferer, D. Raabe, *J. Mater. Sci.* 45 (2010) 6604–6610.
- [31] O. Bouaziz, *Scripta Mater.* 66 (2012) 982–985.
- [32] S. Allain, J.P. Chateau, O. Bouaziz, *Mater. Sci. Eng. A* 387–389 (2004) 143–147.
- [33] L. Chen, H.S. Kim, S.K. Kim, B. De Cooman, *ISIJ Int.* 47 (2007) 1804–1812.
- [34] V. Gerold, H.P. Karnthaler, *Acta Metall.* 37 (1989) 2177–2183.
- [35] S.I. Hong, C. Laird, *Acta Metallurgica et Materialia* 38 (1990) 1581–1594.
- [36] K. Renard, P.J. Jacques, *Mater. Sci. Eng. A* 542 (2012) 8–14.
- [37] K.M. Rahman, V.A. Vorontsov, D. Dye, *Mater. Sci. Eng. A* 589 (2014) 252–261.
- [38] H.K. Yang, Z.J. Zhang, Z.F. Zhang, *Mater. Sci. Eng. A* 622(0) (2015) 184–188.
- [39] I.C. Jung, B.C. De Cooman, *Acta Mater.* 61 (2013) 6724–6735.
- [40] L. Lu, T. Zhu, Y. Shen, M. Dao, K. Lu, S. Suresh, *Acta Mater.* 57 (2009) 5165–5173.
- [41] I. Gutierrez-Urrutia, D. Raabe, *Acta Mater.* 60 (2012) 5791–5802.
- [42] X. Feaugas, *Acta Mater.* 47 (1999) 3617–3632.
- [43] B. He, B. Hu, H.W. Yen, G.J. Cheng, Z.K. Wang, H.W. Luo, M.X. Huang, *Science* 357 (2017) 1029–1032.
- [44] I. Gutierrez-Urrutia, D. Raabe, *Acta Mater.* 59 (2011) 6449–6462.
- [45] H. Wang, Z. You, L. Lu, *Mater. Res. Lett.* 6 (2018) 333–338.